Chapter 2

Nanotubulation from membrane bilayers.

2.1 Summary

Tubule formation from membrane organelles in living cells is extensive and dynamic requiring the energy consuming molecular motors [1, 2, 3]. Such motor proteins can apply forces of the order of a few picoNewtons. Experiments on tubule extension from *invitro* reconstituted endoplasmic reticulum (ER) and golgi membranes have been used to show that the golgi membranes are maintained at a higher tension as compared to the ER membranes [4]. Measurement of forces for constant tubule extension from plasma membranes of living cells has given an understanding of the cell membrane tension regulation with osmotic pressure changes [5]. Force-extension curves obtained for unilamellar vesicles [6] exhibit increase in the force with tubule length when there is no reservoir of membrane available for large tubule extensions.

In this chapter we have studied nanotubulation from multilamellar membrane vesicles using the optical trap. An optically trapped bead is used to extract tubules from cationic vesicles and the displacement of the bead in the trap is measured to estimate the force of tubulation. The design of the optical trap and calibration for position and trap stiffness aredescribed in sections 2.3.1 and 2.3.2 respectively. We have developed a force modulation method based on the intensity modulation of the optical trap, to study frequency dependent dynamics of membrane nanotubules; presented in section 2.3.3. Section 2.3.4 outlines the preparation of multilamellar cationic vesicles using the hydration method. Cationic surfactant molecules di-dodecyl-dimethyl-ammonium-bromide (DDAB) was used for vesicle preparation, since DDAB is know to form fluidic bilayers at room temperature.

In section 2.4.1 we describe our measurements of force for tubule formation from multilamellar vesicles, of diameter ~ 5μm-20μm adhered onto glass microscope cover glass. We observed two regimes in the force-extension curves; an elastic regime with the force increasing sharply with the extension of the tubule (< 5μm) and a saturation regime with the force almost constant at ~ 0.4pN-0.6pN for large extensions (~ 80μm-100μm). The saturation of force suggests the flow of membrane bilayers into the tubule, the multilamellae acting as reservoir of membrane assisting the tubule extension. The

stiffness of the nanotubule and its other characteristics are quantified in section 2.4.2. The tubule recoil curves were recorded and the elastic modulus was estimated.

The dynamics of the tubule-vesicle system was studied using the force modulation optical trap, described in section 2.4.3. The force modulation was achieved by sinusoidal modulation of the trap intensity and hence the bead position in the trap. We observed a frequency dependent response of the tubule to the force modulation. The response amplitude vs. tubule extension curves had well resolved peaks at the threshold of force saturation at these characteristic modulation frequencies.

2.2 Introduction

Membrane bilayers in biology play the role of segregating boundaries, since they are impermeable to water. The cell membrane, nuclear membrane and various membrane organelles like the endoplasmic reticulum (ER), golgi and endosomes are a few examples. Membrane bilayers constitute ampiphilic molecules that have polar head groups and non-polar hydrocarbon chains. Beyond the "Critical Micellar Concentration – CMC" of lipid molecules in water, they form either micellar structure or bilayers (Figure 2.1). The size of the head group and the number of hydrocarbon chains of the lipid molecule determine the structure. The cross-sectional diameter of a lipid is ~1nm and the length depends on the length of the tails. The thickness of membrane bilayer made of single lipid component is ~5nm and the area of the membrane stretches over several tens of microns.

Biological membranes are most often bilayers and they also constitute various membrane proteins, like receptors, ion channels, protein pores etc. This allows signaling and directed transport of molecules across the membrane. Membranes in cells assume various shapes and are highly dynamic as required by a variety of functions they perform. Active budding and fusion of vesicles render the plasma membrane and the ER membranes dynamic. These vesicles are responsible for intracellular transport of cargo proteins and signaling molecules. The transportation of these vesicles is achieved by microtubule based molecular motors anchored to them. In addition to the classical notion of membrane vesicles being the transport intermediates in cells, there is now popularly accepted idea of membrane tubules being involved in intra-cellular and inter-cellular transport.

Membrane tubules have been shown in biological cells to form extensive network and are involved in intracellular transport. Membrane tubules connecting the golgi stacks and, the ER with the Golgi membrane have been shown from electron microscopy and fluorescence microscopy [1]. The tubule networks are made by molecular motors and are associated with the cytoskeleton network. Tubulation has been shown in *invitro* systems to be energy driven and requires cooperative molecular motor activity [2, 3]. A minimal system of Giant Unilamellar Vesicles on microtubule networks and microbeads coated

with Kinesin motors was used to show membrane tubule formation requiring ATP and cooperative activity of Kinesin motors. Such cooperative activity prerequisites a minimum concentration of motors, indicating a mechanism for membrane traffic regulation. Tubular connections acting as transport intermediates between individual cells have been shown. Membrane tubules from plasma membrane and various membrane organelles of cells have been formed using various techniques some of these being hydrodynamic flow, micropipette and optical/magnetic tweezers. Tubule formation from isolated membranes of the Endoplasmic Reticulum and Golgi using optical tweezers has given an estimate of the tension of the isolated ER membranes and golgi membranes [4]. The ER membrane tension has been shown to be greater than that of isolated Golgi membranes by measuring the static tether force. A higher force of 18.6±2.8pN was required to draw tethers from the ER and a lower force of 11.4±1.4pN for the golgi membrane. This would explain the flow of membrane into the Golgi when the ER membrane is fused with the Golgi membrane.

Membrane vesicles and tubules.

Membrane bilayers (comprising of phospholipid or surfactant molecules) do not exhibit surface rigidity and hence do not resist anisotropic stress in the plane of the membrane. As a consequence, in the absence of lateral tension, the sole determinant of membrane shapes is the "membrane bending rigidity". The extraordinary number of shapes that the membranes can assume is a result of their fluidic structure and bending energies. The bending rigidity results due to the fact that the molecules are constrained to be in the surface due to the hydrophobic effects and hence there is a preferred thickness of the membrane and membrane area per lipid molecule. Stretching of membrane would involve decreasing the lipid density in the membrane hence exposing the non-polar hydrocarbon chains to water. The membrane bilayer stretching requires large free energy changes whereas the bending energies are small leading to thermally driven membrane height fluctuations. The relative stretching between the inner and the outer monolayer constituting the membrane, results in the "Membrane Bending Stiffness-k" and depends on the Young's modulus of the membrane. The bending stiffness is scale invariant, independent of the size of the membrane.

Membrane bilayers form closed structures called vesicles to prevent the hydrophobic regions along the edge from being in contact with water. The vesicle formation results due to the edge line energy being greater than the energy required to bend the membrane to form a vesicle with certain curvature. The shape of the vesicle is primarily determined by the bending elasticity of the membrane bilayer. If the edge energy is σ_E, per unit length due to contact between hydrocarbon regions and water, the total energy is proportional to the total edge length. The edge energy scales with size L of the membrane and we have seen that the bending does not depend on the size. Thus for large L the minimum energy conformation of the membrane is that of a closed vesicle.

A point-like force on such a vesicle leads to the formation of membrane tubules that are cylindrical in shape and of diameter below optical resolution. Waugh and Hochmuth [7] derived the relations for the dependence of the force of tubule formation, the tubule radius and the membrane bending rigidity (discussed later). For a cylindrical tubule of radius R=50nm and the membrane bending rigidity $k_c=10^{-19}$J, the force ~6.28pN. This is of the order force that can be applied by molecular motor proteins that form membrane tubules.

Optical tweezers have been used to study the cell membrane tension regulation in biological cells with changes in extracellular conditions by measuring the static force required to sustain a certain tubule extension [5]. The

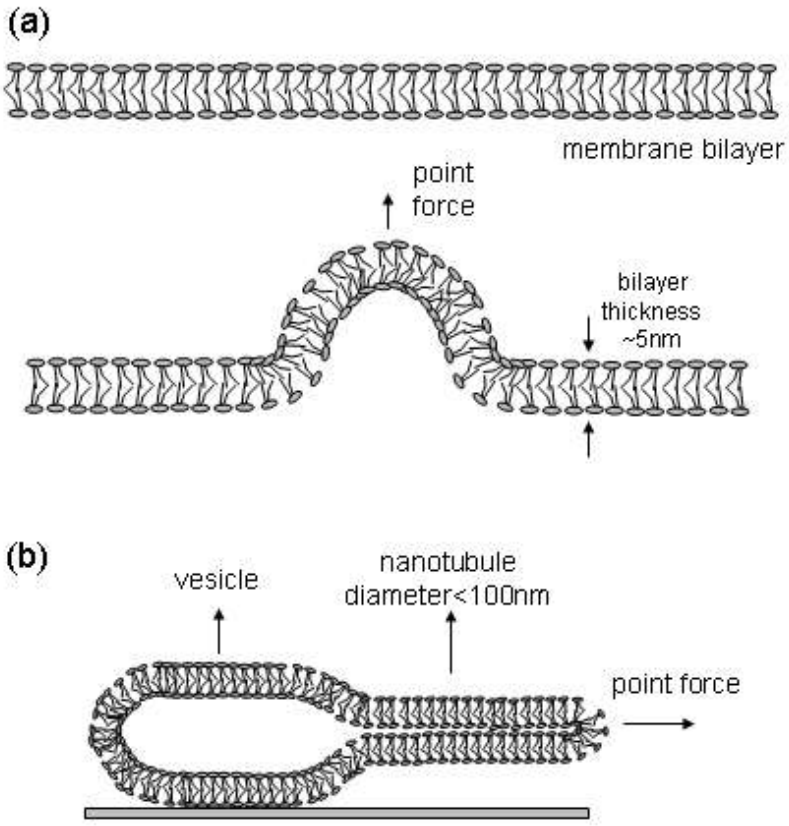

Figure 2.1

(a) Schematic of membrane bilayer with the hydrophobic regions sandwiched between the hydrophilic head groups. The thickness of the bilayer is ~5nm and the bilayers extend to tens of micromters in area. A point force on the bilayer leads to change in the membrane shape locally and eventualy formation of a nanotubule. **(b)** Schematic of a vesicle and a nanotubule formed due to the point force.

membrane-cortical adhesion for a variety of biological cells and variations in cell membrane tension with disruption of actin network in these cells was also studied. The relation between force of tubule formation, the radius of the tubule and membrane tension as derived by Waugh and Hochmuth [7] was used in the above experiments. The measured force on the bead (tether force) did not depend on tether length over a wide range of tether lengths, indicating that a reservoir of membrane and not elastic stretching of the plasma membrane provides the membrane for tether extension.

Tubule extraction from cell membrane has been used to estimate the tension of the membrane using shear flow or micropipette based aspiration experiments. Such experiments have also been performed on membrane vesicles (mainly unilamellar) to avoid the influence of the cytoskeleton-membrane interaction forces on the measurements. The radius of the optically invisible tether/tubule can be estimated in these micropipette experiments [8, 9]. A glass micropipette is used to aspirate a section of the membrane vesicle and a glass bead adhered to the vesicle outside the micropipette is used to pull out a membrane tubule. The section of the membrane inside the micropipette acts as a reservoir for the tubule length extension. The change in length of the membrane vesicle protrusion inside the micropipette and the radius of the micropipette itself can be used to determine the radius of the tubule knowing the length of the tubules from the position of the glass bead with respect to the vesicle. These experiments have provided an estimate of ~20nm for the radius of the membrane tubule and the radius varies inversely with the force. The membrane tension times the circumference of the tubule is equal to the tubule radius [9].

A point-like force on membrane bilayers results in the formation of a cylindrical tubule, the radius of the tubule being inversely related to the applied force with the bending stiffness being the proportionality factor, Figure 2.1. The membrane bending stiffness determines the intrinsic deformability of membrane bilayers. Hence, this property of the membrane is relevant to processes involving changes in curvature in biological membranes, for example, membrane tubule formation, cell division, endocytosis, exocytosis etc. Such tubule formation from artificial membrane vesicles has been used to estimate the bending stiffness of the membrane by optical tweezer force measurement and micropipette aspiration technique [10]. The radius of the tubule and the

force required for tubule formation is determined by the membrane bending stiffness and the membrane tension, for a point-like force. The above mentioned experiments use a bead (microsphere) adhered onto a unilamellar membrane vesicle to pull out nanotubules. The area of contact between the membrane and the bead controls the radius of the tubule and hence the force of tubule formation [11]. The initial deformation due to the force leads to a catenoid shape of the membrane after which the membrane bilayer assumes the shape of a tube coexisting with a spherical shaped vesicle. We have studied such tubule formation from artificial vesicles of charged surfactant molecules using an optical trap. The dynamics of such tubule formation was probed using a force-modulation technique to find the frequency dependent enhanced response of the vesicle-tubule system to the periodic forcing.

2.3 Materials and Methods

2.3.1 Construction of the optical trap.

The optical trap was constructed on an inverted microscope (IX70 Olympus, Japan) and an infra-red laser (1064nm, Nd-YAG, 200mW, Coherent, USA), Figure 2.2. A visible laser backscattering method is used to probe the displacement of the 2μm latex particle from the center of the trap and hence measure the force acting on the bead. The laser beam (diameter = 0.9mm at the source) was expanded using a 7× beam expander (Model CWBX-6.0-7X-1064; CVI Laser Corporation, USA) into a beam of diameter 6.3mm.

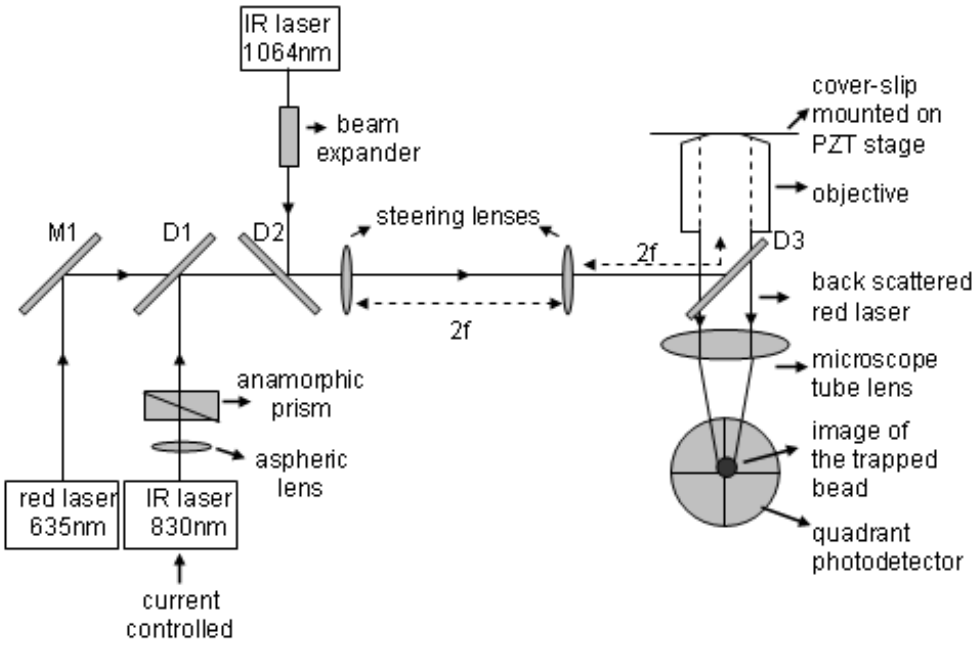

Figure 2.2

Design of the experimental setup. An inverted optical microscope is used to build the optical trap. The 830nm (GaAlAs-diode laser) and the 1064nm (NdYAG semiconductor laser) are the trapping lasers and the 635nm red laser is used for detection of the bead position in the trap. D1, D2 (Model 9000RSP, Chroma, USA; reflectance of the infrared laser (1064nm) is maximized) and D3 (Model 775dcspxr; Chroma, USA; optimized to reflect the IR lasers) are dichroic mirrors.

The beam diameter was increased using a beam expander to ensure minimum spot size, the spot size being inversely dependent on the beam diameter. This 6.3mm diameter trapping beam just overfills the back-focal aperture of the objective, so designed to avoid changes in the beam diameter when the beam is steered in the objective focal plane. The steering of the beam is achieved by a telescopic arrangement of two lenses of equal focal lengths. The distance between the two lenses and the distance between the second lens (from the laser source) and the back-focal plane of the objective are equal to 2×focal length of the lenses. This arrangement creates conjugate planes, one at the common focal plane of the two lenses and the other at the focal plane of the objective. Steering the first lens (from the laser source) would move the focal spot at the centre of the lenses as well as the focal spot of the objective lens. Such an arrangement thus allowed us to move the laser focal spot and hence the trapped bead in the object plane. The high numerical aperture objective (planapo 100×, N.A.=1.4, oil immersion, Olympus, Japan) was used to focus the trapping infra-red laser beam into a diffraction limited spot of size $\omega=1.22\lambda f/D$, where λ is the wavelength of the laser, f is the focal length of the objective lens and D is the diameter of the laser beam. The focal spot size for the optical trap was ~500nm in diameter. The red laser (wavelength 635nm) aligned along the infrared laser was used for the detection of the bead position in the optical trap. The two lasers were mixed at the dichroic mirror D2 (Model 900DRSP, Chroma, USA) as shown in Figure 2.2. The dichroic mirror D2 is designed such that the reflectance of the infrared laser (1064nm) is maximized. The lasers are reflected into the objective of the microscope by the dichroic mirror D3 (Model 775dcspxr; Chroma, USA), optimized to reflect the IR lasers. The displacement of the bead in the trap is detected by focusing the backscattered red laser, 635 nm wavelength (5mW power, Model 31-0128; Coherent Inc., CA, USA) on to a Quadrant Photodiode (SPOT4D; UDT Instruments & Model 431 X-Y Position Indicator; UDT Instruments, USA) [13]. Data acquisition and analysis was done using DAQ card (PC-MIO-16XE-10, National Instruments, USA) and LabVIEW (Version 5.1, National Instruments, USA). Backscattering of the red laser by the trapped 2μm diameter polystyrene bead (Catalog # 13627, Polysciences, Inc., USA) is focused onto a quadrant photodiode (SPOT4D; UDT Instruments, USA) to detect the displacement and hence estimate the force on the bead.

2.3.2 Calibration of the photodetector and the optical trap.

The outputs of the photodetector are four currents corresponding to the four quadrants of the photodetector. The amplifier was used to convert the currents to appropriate voltages and obtain the differential voltages corresponding to each axis of the detector. If V_A, V_B, V_C and V_D are the four voltages then the voltages corresponding to the two axis of the detector are given by the differential voltage signals

$$V_x = \frac{(V_A + V_D) - (V_B + V_C)}{V_A + V_B + V_C + V_D} \quad \ldots\ldots\ldots \quad (2.9)$$

$$V_y = \frac{(V_A + V_B) - (V_C + V_D)}{V_A + V_B + V_C + V_D} \quad \ldots\ldots\ldots \quad (2.10)$$

To obtain the corresponding distance change we used a bead stuck to a glass cover-slip. The bead was moved ~4μm using the PZT stage (3 axis PZT stage, Model P577.3CL, with servo controller Model E-509.C3; Physik Instrumente, Germany) and the corresponding voltage change was acquired as shown in Figure 2.3(a). The detector responds linearly as long as the bead image is within the active area of the detector ($4mm^2$), beyond which the voltage decreases, Figure 2.3(b). The linear region, refer Figure 2.3(c), is used to calculate the slope which gives the detector calibration. The appropriate calibration for the X and Y direction were performed for all our experiments. A 1volt output from the quadrant detector amplifier corresponds to ~0.6μm displacement of the bead for most of the data obtained as shown in Figure 2.3 (c).

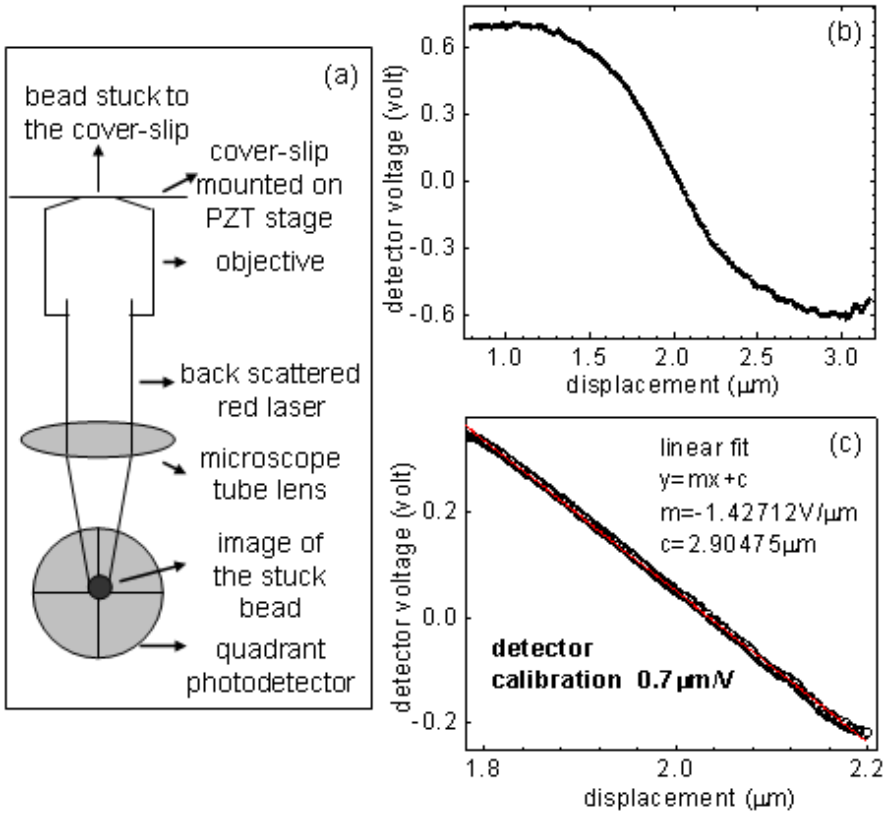

Figure 2.3

(a) Schematic of the photodetector calibration. The bead was moved ~4µm using the PZT stage and the corresponding voltage change was acquired as shown in **(b)**. **(c)** the linear region is used to calculate the slope which gives the detector calibration; 1volt output from the quadrant detector amplifier corresponds to ~0.6µm displacement of the bead.

The variance in the fluctuations of the trapped bead was used to calibrate the trap stiffness, $k_{trap}=k_BT/var(x)$. The voltage time series from the quadrant detector amplifier was measured at an acquisition rate of 2000 points/s. The position time series in "nm" was obtained by using the photodetector calibration as discussed above. In our case, for the 1064nm wavelength laser with power 200mW, the standard deviation was ~50nm for a 2μm bead and hence $k_{trap}=1.6\times10^{-6}$N/m, Figure 2.4.

2.3.3 Force modulation optical trap.

Force modulation optical trap was achieved using a current controlled semiconductor diode laser (wavelength 830nm, GaAlAs diode, model 5430; SDL Inc., USA) and controller (Model LDC-3724B; ILX Lightwave Corporation, USA) as shown in Figure 2.3. The uncollimated beam from the semi-conductor laser was collimated using an aspheric lens (Model C240TM; Thorlabs, USA) and circularized using the anamorphic prism pair (Model AP-6X-10.0; CVI Laser Corporation, USA). The dichroic mirror D1 (Model 775dcspxr; Chroma, USA), optimized to reflect 830nm wavelength was used to mix the 830nm and the 635nm laser beams. A sinusoidal signal of appropriate amplitude and frequency from a function generator (Model DS345; Stanford Research Systems, USA) was used to modulate the intensity of the infrared laser; a 1volt at the controller input changes the controller current by 20mA.

For the frequency sweep measurements, a 0.5V sinusoidal signal from the DAQ board (model: PCIMIO16XE-10; National Instruments, USA) generated at different frequencies by Lab View (version 5.1; National Instruments, USA) programming was connected to the laser diode controller for modulating the trap intensity. The response amplitude dependence on the tubule extension was measured, by a lock-in amplifier (Model SR830; Stanford Research Systems, USA), whose reference output is connected to the laser diode. The output of the quadrant photodiode amplifier (X-Y Position Indicator Model 431; UDT

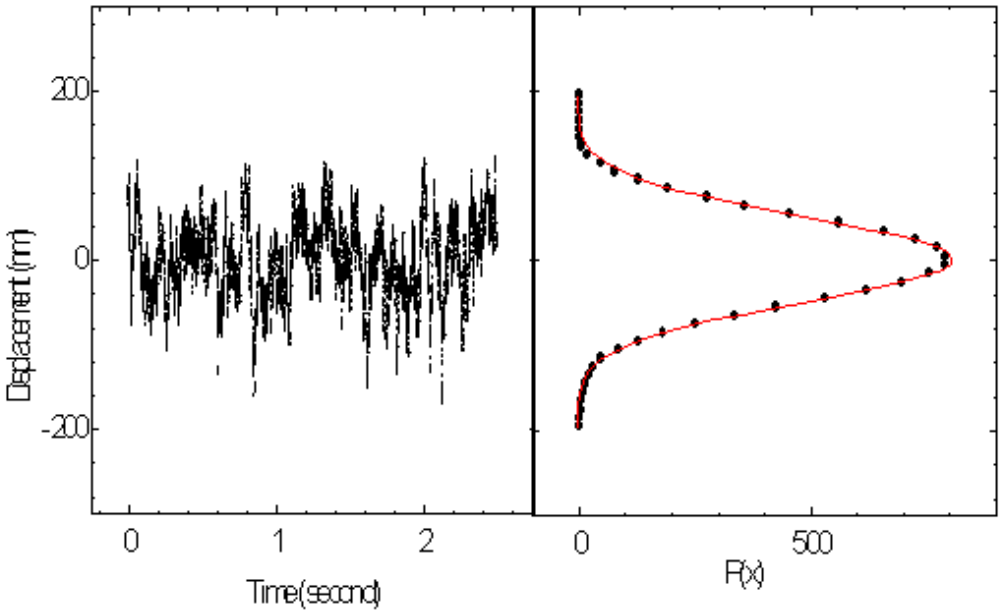

Figure 2.4

A typical time series of the position of trapped bead. The position probability histograms are fitted to a Gaussian distribution to obtain the variance, and the trap stiffness is calculated using $k_{trap} = \frac{k_B T}{\langle \Delta x^2 \rangle}$. For a variance of 2445nm^2 the trap stiffness was calculated to be 2.6×10^{-6}N/m.

Instruments, USA) is fed to the lock-in amplifier to measure the response amplitude at the modulation frequency (1Hz to 200Hz). The amplifier for the photodetector gives two outputs corresponding to the bead displacement in perpendicular directions in the focal plane (V_x and V_y). We chose the direction in which the tubule is pulled out. This voltage was fed into the lock-in amplifier that convolutes the signal with the reference signal to obtain the response of the bead at the frequency of modulation. The lock-in amplifier gives the imaginary (V_I) and real (V_R) components of the response at the modulating signal frequency, from which the amplitude ($V_A = (V_R^2 + V_I^2)^{1/2}$) and the phase ($\tan^{-1}(V_I/V_R)$) of the bead oscillation are calculated.

An appropriate integration time was chosen at each step of extension, in order to integrate out the Brownian fluctuations of the bead. In our experiments, with the intensity modulated trap constructed using the 830nm laser, the dc trap stiffness is ~1×10^{-5}N/m (for 40mA laser diode current) and varies in the range of 0.6×10^{-5}N/m to 1.8×10^{-5}N/m with the modulating signal of 0.5V. The data was acquired using the DAQ board and LabView 5.1.

2.3.4 Multilamellar vesicle preparation.

The cationic surfactant didocyl-dimethyl-ammonium-bromide (DDAB) (molecular weight = 630.96), with a bromide counter-ion forms multilamellar swollen lamellar phase at room temperature at weight percentage >10% [14]. The DDAB is mixed in 100% ethanol at a concentration of 20mM (weight percentage 500%). 100 μl of this solution is spread on a 1"×1" clean and dry teflon piece and incubated in the oven at a temperature of 50°C over 8hrs. 500μl of PBS (Phosphate Buffer Saline, 2× buffer) at pH 7.4 is added to this so that the final lipid concentration is 4mM. The solution is sonicated for one hour to get vesicles with sizes ranging from 2μm to 50μm. It was taken care that the sonication bath was at room temperature during sonication. An increase in the temperature of the water in the sonicator resulted in low yield of vesicles. The vesicles were stored at 4°C and used over two weeks after which time they degrade. For fluorescence imaging of the membrane tubules Fluorescein Isothiocynate (Excitation

maximum 497nm and Emission maximum 521nm) was mixed to PBS buffer (2×, pH 7.4) at 2nM concentration before sonication. This method of formation gives multilamellar vesicles. The measured area per head of the DDAB at these concentrations is ~1nm^2 [14].

2.4 Results and Discussions

2.4.1 Force-Extension curves of tubule formation from membrane vesicles.

Membrane nanotubule formation was studied on the multilamellar vesicles prepared as described in the methods section 2.3.3. The glass cover-slip used for the sample well was cleaned in 100% ethanol in an ultra-sonicator for ~30min and dried at 100°C in an oven. The sample well was made using a rubber O-ring fixed with paraffin wax. 50μl of vesicle solution was transferred onto sample well and the cover-slip was then mounted on a piezoelectric (PZT) stage, fixed onto the microscope. The sample was washed (ten times with PBS pH6.0, 1× buffer) to remove free vesicles. The PBS 1× buffer concentration was used for washing the sample well to ensure that the vesicles, prepared in PBS 2× buffer and hence heavier, settle onto the glass cover-slip. The sizes of the vesicles ranged from ~2μm-50μm. The sample also consisted of aggregates, sometimes the vesicles being connected by tubules. The bright field image of the vesicle with the trapped bead attached is shown in Figure 2.5. The multilamellar vesicles were visible under the ordinary bright field microscope.

We measured the force-extension curves for tubule formation from multilamellar membrane vesicles using the optical trap. 2μm carboxyl coated poly-beads (Catalog #13627, Polysciences, Inc., PA, USA) suspended in PBS pH6.0 buffer were added to the sample well (10^6beads/100μl sample volume). For the experiment, an isolated vesicle firmly adhered on the cover-slip (diameter in the range of 5μm-10μm) was selected. The optically trapped bead was adhered onto the vesicle achieved by non-specific electrostatic interactions between the carboxyl-groups on the bead surface and the cationic surfactant molecules. The PZT stage was then moved in steps of 10nm away from the

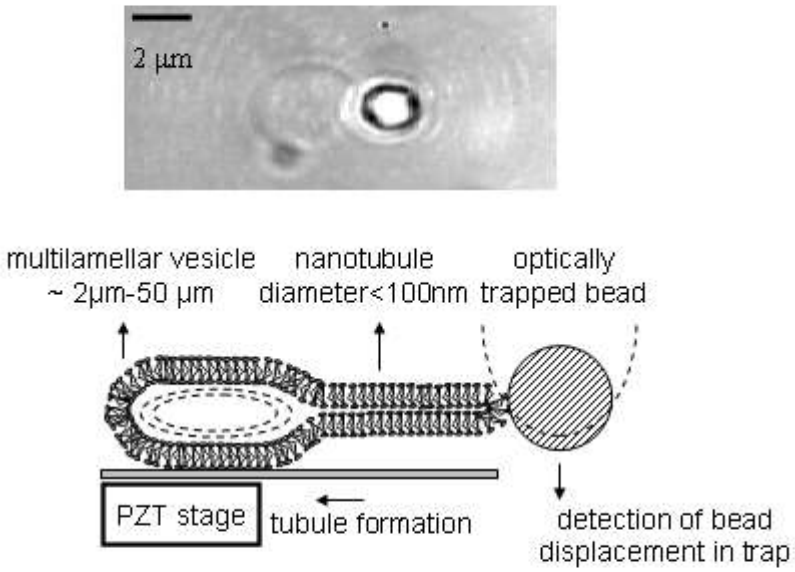

Figure 2.5

Picture of the multilamellar vesicle with an optically trapped bead adhered onto it (top panel). A cartoon (not to scale) of tubule formation from a vesicle using an optical trap is also shown.

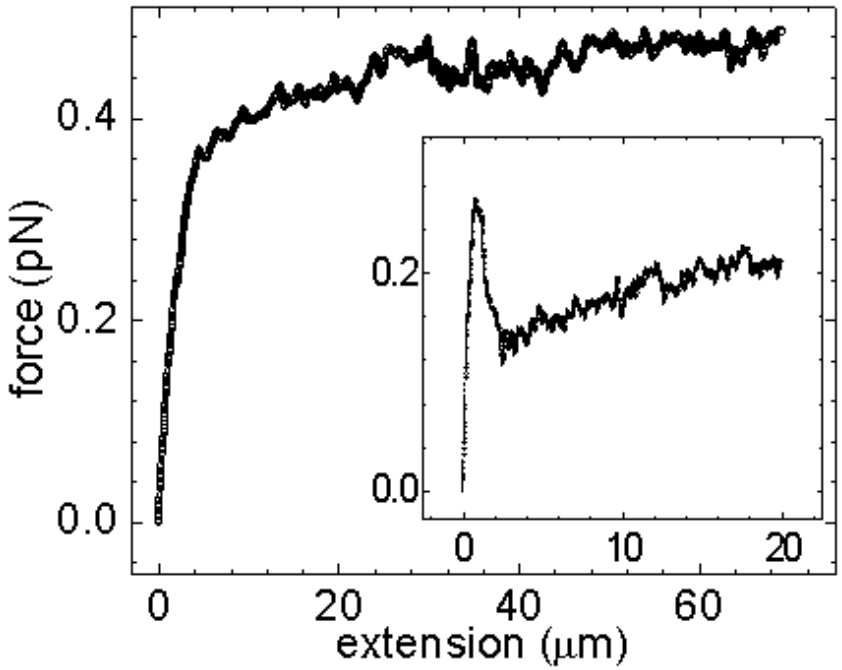

Figure 2.6

Force extension curve for nanotubules formation from a multilamellar vesicle. The trap stiffness was 1.6×10^{-6}N/m. The force saturates at ~0.4pN followed by a soft regime. The characteristic spring constants (dF/dX) in the two regimes are; ~1×10^{-3}pN/nm in the stiff elastic regime and ~2.5×10^{-6}pN/nm in the soft regime. Inset to the figure shows force extension curves obtained in about 30% of cases where a negative force jump is observed at the threshold of force saturation.

trapped bead to form the tubule. The bead displacement from the trap centre was measured using the quadrant photodetector. A time series of the bead position was recorded, 100 points at an acquisition rate of 2kHz. The mean of the time series was calculated to obtain the bead position in the trap for each extension. The force on the trapped bead due to tubule formation was calculated using the Hooke's law assuming a harmonic potential for the trap. The force is given by $F=-k_{trap}\times\Delta x$, where k_{trap} is the trap stiffness and Δx is the displacement of the mean position of the bead in the trap. The force extension curve was recorded as a function of the tubule extension, Figure 2.6. Typical recording time was ~10s for 50μm extension of the tubule.

The experimentally measured force extension curves reveal a sharp increase in the force required to pull out a tubule from the multi-lamellar membrane vesicle. Beyond a threshold force ~0.6pN, however, the tubule length can be increased to several tens of microns with <0.2pN increase in the force. The threshold value of force saturation varies between 0.4pN to 0.8pN for different vesicles. In 30% of the vesicles, we also find that beyond the threshold force, there is a negative slope in the curve before the onset of tubulation as shown in inset to Figure 2.6. The sharp reduction in the force at the threshold is discussed later. In Figure 2.7 we plot the force extension curves recorded during tubule extraction and retraction. As clearly seen, the force-extension curves display no hysteresis in the force of tubule formation and retraction, the velocity of tubule formation being ~200nm/s. At higher velocities we encountered PZT stage hysterisis.

The force extension curves of tubule formation were found to be independent of tubule extraction rates. Figure 2.8 shows the force-extension curves for extraction rates of 500nm/s, 200nm/s and 20nm/s (maximum rate in our setup being 5μm/s). The saturation regime is characteristic of flow (tubulation) of the multi-lamellar vesicle material under an applied tension beyond the threshold force. As noted above, the flow was independent of the rate of tubule extraction.

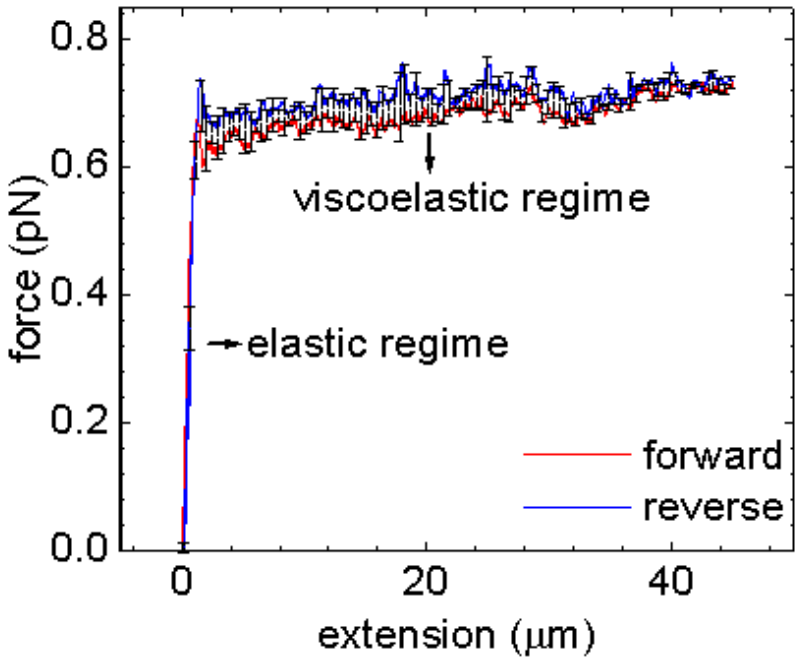

Figure 2.7

The force extension curves for tubule formation are reversible. The force curve is plotted for tubule extraction (forward-red line) and retraction (reverse-blue line) on the same vesicle. The force curves do not exhibit hysteresis in the formation and retraction of tubule. The stiff elastic regime and the soft viscoelastic regime are marked by arrows.

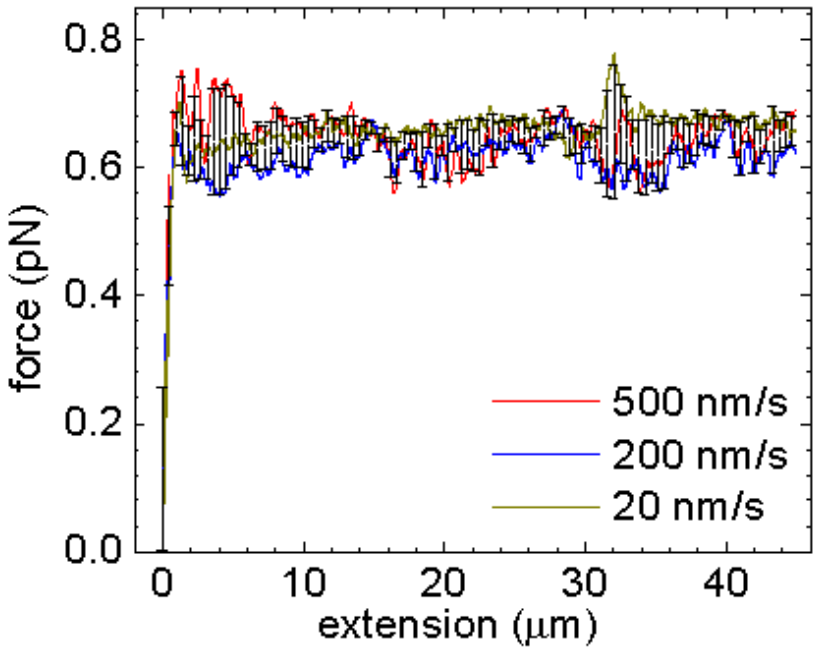

Figure 2.8

The force extension curves for tubule formation are plotted for different rates of tubule extraction (500nm/s-red line, 200nm/s-blue line and 20nm/s-dark green line). The initial stiff elastic regime and the soft viscoelastic regime are independent of the rate of pulling.

The nature of the curve does not change when the tubule is formed many times and is very reproducible, as shown in Figure 2.9.

Two regimes can be seen in the force extension curve, the initial stiff elastic regime where the force increases sharply, and the late saturation regime, which is considerably softer. The elastic regime of the force-extension curve is shown in Figure 2.10. The increase in the force in this regime is due to the energy required to bend the planar membrane bilayer. The elastic regime is clearly non-linear and varies over different vesicles due to change in the membrane tension and the bead-membrane adhesion area. The elastic regime shows characteristic serrations in the F-X curve as shown in Figure 2.10, where the raw data is smoothened by an adjacent eight point averaging. An average number of two or three such serrated jumps (of the order of 0.1pN as shown by arrows in Figure 2.10) were observed over different vesicles. The force extension curve is robust and reproducible, but the fine structures (serrations) are not reproducible in detail, although serrations appear in each case. Explanation for the observed serration may be (a) stick-slip motion between the bilayers of the multi-lamellar vesicle during tubulation or (b) successive breakages of the vesicle-bead adhesive contacts. The characteristic spring constants (dF/dX) in the two regimes are vastly different; ~1×10^{-3}pN/nm in the stiff elastic regime and ~2.5×10^{-6}pN/nm in the soft regime (in the linear approximation). The free energy of the membrane for a unilamellar vesicle can be written as

$$E = \int \frac{B}{2} (2H)^2 dA + \sigma A - pV - F_t L_t$$

where, B is the bending stiffness, H is the mean curvature of the membrane, A is the surface area of the membrane, p is the difference between the inside and the outside pressure of the vesicle and L is the end-end length of the vesicle for a point force F [15]. For a cylindrical tube of length L and radius R the free energy for p=0 may be written as

$$E_{tubule} = \left(\frac{B}{2R_t^{\,2}} + \sigma \right) 2\pi R_t L_t - F_t L_t$$

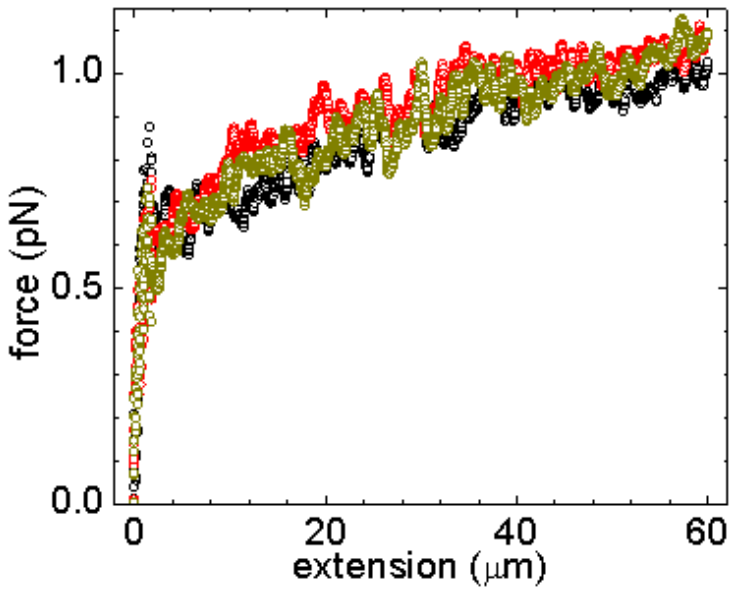

Figure 2.9

The force extension curves of tubule formation are reproduced over many times of tubule formation. Both the stiff elastic and the soft viscoelastic regimes are reproduced.

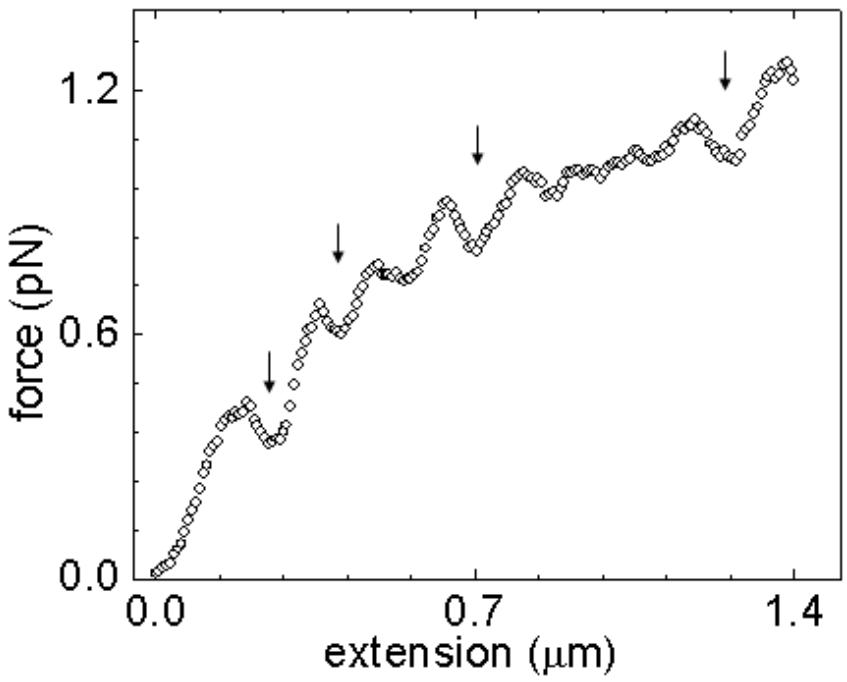

Figure 2.10

The stiff elastic regime of the force extension curve for tubule formation. The elastic regime exhibits a stiffness of ~1×10^{-3}pN/nm. We observe serrations in the force curves of ~0.1pN, in all the curves measured.

The membrane tension works towards reducing the radius of the tubule for an applied point force whereas the bending stiffness tends to increase the radius. The free energy is hence minimized with respect to the radius and the length of the tubule.

$$\frac{dE_{tubule}}{dR} = 0$$

and

$$\frac{dE_{tubule}}{dL} = 0$$

to obtain the equilibrium radius of the tubule for a constant tubule force F_t [16];

$$R_t = \sqrt{B/2\sigma}$$

and

$$F_t = 2\pi\sqrt{2\sigma B}$$

The force on the membrane tether at a constant tether length L_t and radius R_t is determined by the membrane bending stiffness B, given by $F_t=2\pi B/R_t$ [7]. This relation has been used to estimate the membrane bending stiffness to be $\sim 1\times10^{-19}$Nm for SOPC unilamellar vesicles, using the micropipette based suction mechanism [10]. In this experiment the vesicle was held under pressure in the micropipette and a glass bead adhered to the vesicle outside the micropipette was allowed fall under gravity by releasing the pressure in the micropipette. The force on the bead was calculated knowing the size and density of the bead. The radius of the tether is obtained by measuring the decrease in the length of the cylindrical section of the vesicle inside the micropipette, given that the area and volume of the vesicle is constant. The tether formation experiments used to estimate the membrane bending stiffness or the membrane tension of phospholipid vesicles have assumed absence of membrane in-plane stretching during tubule formation or extension. This assumption is valid since as discussed before the stretching of the membrane involves greater energy than bending the membrane.

The initial increase in the force in our experiments results as a consequence of the bending of the membrane bilayer due to the force applied. The bending of bilayer requires relative expansion of one of the leaflets of the bilayer with respect to the other, which determines the membrane stiffness [17]. This bending stiffness is determined by

the shape of the lipid headgroup forming the bilayer, the chain length, temperature and the ion concentrations in the solution. The initial change in curvature to form the tubule hence results in an increase in the force. Once the cylindrical tube is formed there is a decrease in the force, owing to relaxation of the vesicle to spherical shape, as is observed in about 30% of our force-extension curves. Such decrease in the force is also reported for tubule formation from unilamellar vesicles [6, 18], also measured by using an optical trap. The magnitude of the overshoot depends on the area of contact between the bead and the membrane [11]. Most of the force-extension curves measured by us did not show this overshoot in force, suggesting that the nanotubulation in our case results due to a mechanism exclusive to just a change of shape of the membrane.

The equilibrium radius of the tubule for a fixed extension and assuming point force application is hence determined by the membrane tension for a fixed bending stiffness. For a unilamellar vesicle the tubule extension at a constant force is possible until the excess area of the vesicle is drawn into the cylindrical section. Beyond which increase in the length of the tubule requires an increase in the force to be applied [6]. When the excess area is provided by a reservoir of membrane, as is the case in micropipette based experiments and tubulation formation from cells, the force of extension remains constant [18, 19]. In our force-extension curves we observe that after formation the tubule can be extended to very large extensions at constant force, indicating a reservoir of membrane available for extension. We suggest that the extension of the tubule at constant force is due to the flow of membrane material from the different layers of the multilamellar vesicles, into the tubule. The absence of force jump for the cylindrical tubule formation also suggests such membrane flow between bilayers leading to very long tubules. We studied the tubule properties as described in the next section.

2.4.2 Stiffness of the membrane tubule.

The membrane tension of vesicles was characterized by monitoring the fluctuations of the trapped bead attached to the vesicle as shown in Figure 2.11. The position time series of the trapped bead was recorded when (a) free in the trap (b) adhered onto the vesicle and (c) adhered at the end of the tubule pulled to a length of 30μm. The

time series was recorded at an acquisition rate of 2kHz and the histograms plotted for each of the above cases. The gaussian fits to the histograms were used to obtain the standard deviation of the bead position time series. The standard deviation values are ~51nm for the trapped bead, ~37nm for the trapped bead adhered onto the vesicle and ~54nm for the trapped bead adhered to the tubule of length 30μm. The standard deviation values of the trapped bead and the bead adhered to the vesicle were used to estimate the vesicle tension. A floppy vesicle would result in a higher value of the standard deviation as compared to a vesicle of greater tension.

The system of trapped bead adhered onto the vesicle is equivalent to two springs in parallel, one due to the membrane and other due to the trap. The effective spring constant is given by, $\frac{1}{\langle \Delta x_{eff}^2 \rangle} = \frac{1}{\langle \Delta x_{trap}^2 \rangle} + \frac{1}{\langle \Delta x_{memb}^2 \rangle}$. Using the equation $k\langle \Delta x^2 \rangle = k_B T$ and the above equation we calculate $k_{eff}=3\times10^{-6}$N/m and $k_{trap}=1.4\times10^{-6}$N/m, the membrane tension $\sigma=2.6\times10^{-6}$N/m. The radius of the tubule was estimated using the above order of magnitude estimate of the membrane tension and the threshold force of tubule formation. The tubule radius, $R_t=F_t/\pi\sigma=80$nm, where $F_t=0.6$pN is the threshold tubulation force and $\sigma=$

2.6×10^{-6}N/m is the membrane tension. From the tubule radius r=80nm and the tubulation force F_t~0.6pN, we can also estimate the membrane bending stiffness

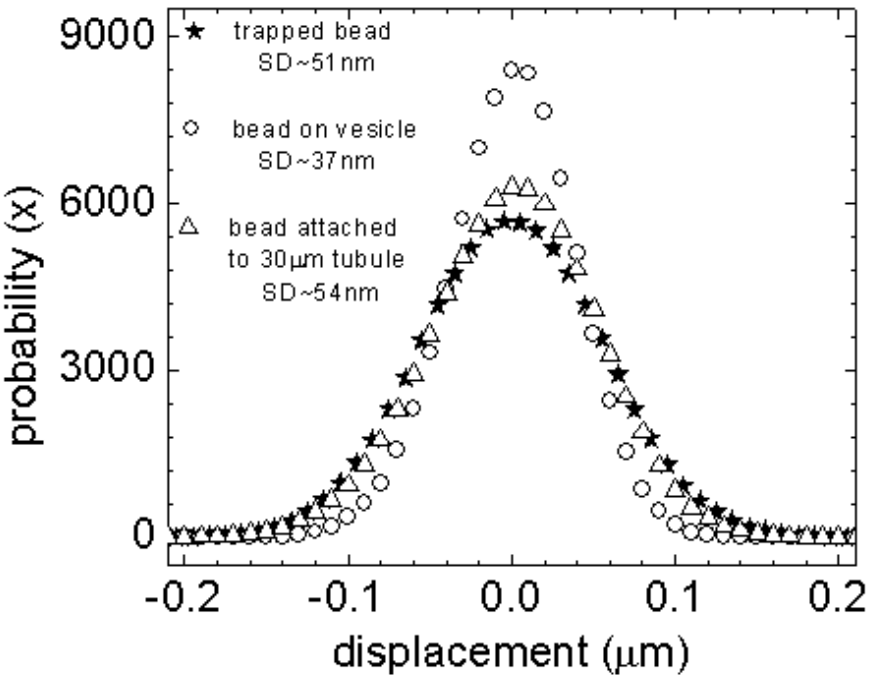

Figure 2.11

Probability distributions of the position fluctuations of the trapped bead (closed stars), trapped bead adhered onto the vesicle (open circles) and trapped bead attached to a tubule extended to a length of 30μm (open triangles). Gaussian fits to the distributions give standard deviation values of 51nm for trapped bead, 37nm for trapped bead adhered to the vesicle and 54nm for the trapped bead attached to the end of the tubule of length 30μm.

$B=FR_t/2\pi\sim8\times10^{-21}$Nm. This estimate is an order of magnitude smaller than the bending stiffness of $\sim10^{-19}$Nm estimated for SOPC membrane bilayers (see previous section) [10]. However these numbers calculated are approximate since the equations describe a unilamellar vesicle. The tubulation force ~0.6pN that we have measured is also an order of magnitude smaller than the values of ~10pN or higher measured for tubule formation from unilamellar vesicles held under pressure at constant tension. The bending stiffness described above does not account for the area expansivity and the relative area expansivity between the two monolayers of the bilayer into account. The contribution of the relative area expansivity is discussed in reference [20].

The low tubule force of <1pN measured suggests that the multilamellar vesicles used for our experiments have a low tension. The low tension could be due to high surface area to volume ratio of the vesicle. Alternatively the excess area may be provided by the many bilayers of the multilamellar vesicle setting the low membrane tension. The latter is probably the case since the force of tubulation saturates after the threshold force of formation. We use the tubule extension force (f~0.17pN), the extension length δL_t=75μm, the initial length L_t=5μm and the radius of the tubule (R_t~80nm) to calculate its Young's modulus $Y=fL_t/\pi r^2\delta L_t\sim0.5$Pascal.

Figure 2.12 shows plot of the recoil time of a tubule, which is measured by switching off the trap at a tubule extension of 34μm (limited by the imaging window of our setup). The images of the bead recorded at video rate are digitized to get the recoil time of the tubule-tethered bead. Typical recoil times for different tubules are of the order of 6s. A linear regime is observed in the initial phase of the recoil, which tapers of as the tubule approaches the vesicle. The terminal velocity (v = 8.8μm/s) is estimated using the linear regime by approximating the bead recoil movement to be in quasi-static equilibrium. The recoil force, $F_{recoil} = F_{drag} = 6\pi\eta av = 0.17$pN (where 'η' is the viscosity, 'a' is the bead radius and 'v' the terminal velocity) is consistent with the tubule extension force. The slope of the recoil decreases almost to zero before the bead reaches the vesicle edge.

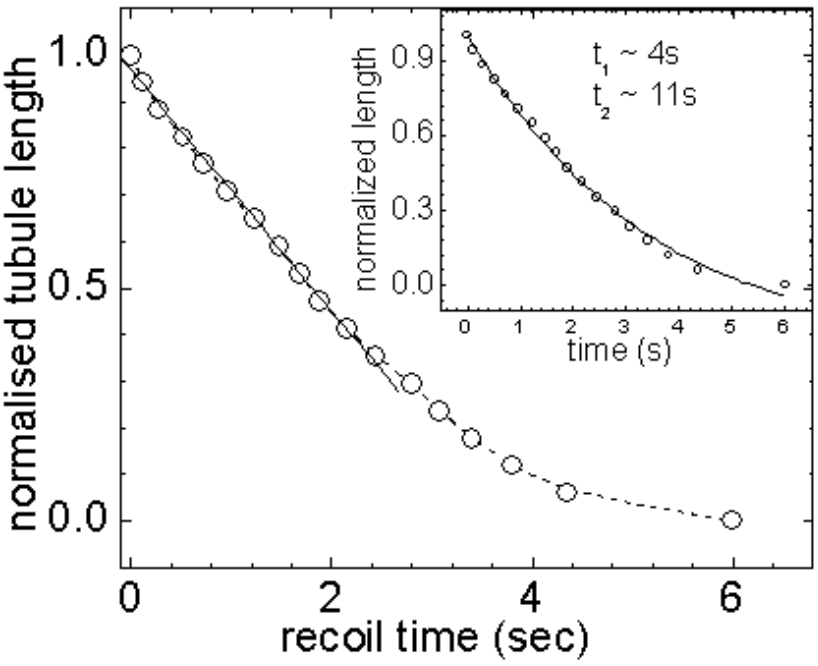

Figure 2.12

The recoil dynamics of the membrane tubule of length 34µm, released by switching of the trap. The linear part of the recoil curve gives the terminal recoil velocity of ~8.8µm/s. Inset to the figure shows a two-time scale exponential decay fit to the recoil curve giving time scales of ~4s and ~11s.

Retraction of tubules have been studied for unilamellar vesicles [21] and found to depend on the membrane tension and the extrusion velocity. In the above referred experiments the retraction length was found to be linearly dependent on the time for low extrusion velocities and the linearity was independent of the membrane tension. The curve exhibited non-linear (more logarithmic) behavior for high extrusion velocities. The retraction curves measured in our experiments fit to an exponential decay with two decay time scales of ~4s and ~11s, inset to Figure 2.12.

We extracted the effective potential seen by the bead during the tubule formation from the experimental force-extension curves as shown in Figure 2.13. The effective potential, which is the sum of the trap potential and the tubule potential, does not vary with the rate of tubule formation. The bead is displaced from the trap center due to the force of tubulation of the vesicle. Hence, the actual length of the tubule is the difference between the distance moved by the vesicle bearing PZT stage and the displacement of the bead in the trap. Since, however, the tubule length is of the order of micrometers while the displacement of the bead is of the order of nanometers, we approximate the length of the tubule to the distance moved by the PZT stage. (The optically trapped bead is just a probe then to monitor the tubule extension). Thus, integrating the rising part of the curve gives us the potential plotted in Figure 2.13. The effective potential U_{eff} seen by the bead is a sum of the potential arising due to trap U_{tr} (harmonic) and the tubule extension U_{tb} (anharmonic). As can be clearly seen, we observe steps in the effective potential corresponding to the serrations in the elastic regime of the force extension curves. The operating point on the force-extension curve so obtained now determines the dynamics of the tubulating membrane as discussed below.

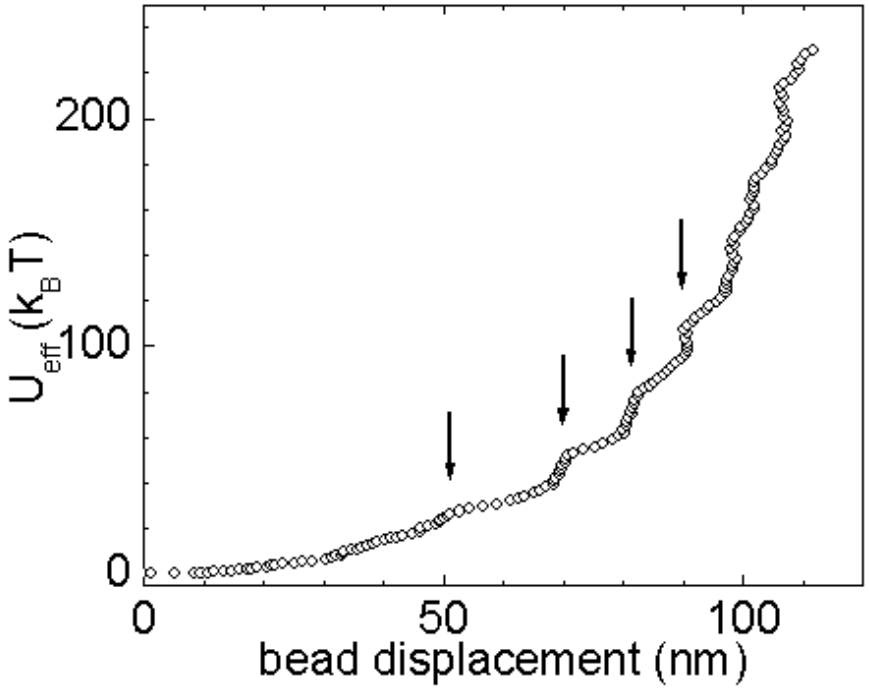

Figure 2.13

Integrating the rising part of the curve gives us the potential due to the trap-vesicle system. The effective potential U_{eff} seen by the bead is a sum of the potential arising due to trap U_{tr} (harmonic) and the tubule extension U_{tb} (anharmonic). As can be clearly seen, we observe steps (marked by arrows) in the effective potential corresponding to the serrations in the elastic regime of the force extension curves.

2.4.3 Dynamics of membrane tubulation.

Frequency dependence of the tubule-vesicle system.

The force extension curves measured for tubulation were independent of the rate of tubule formation and exhibited no hysteresis for the experimentally feasible rates of tubule extraction. The rate or frequency dependence of the tubule formation from a multilamellar vesicle was studied using an optical trap force modulation method. The coupled system of the multi-lamellar membrane tubule
and the optically trapped bead was probed for its dynamics (for frequency response) by weakly modulating the optical trap stiffness at chosen frequencies that creates an alternatively shallow and deep potential well for the bead to move in. The bead is displaced from the trap center due to the force of the tubule coupled to it. The displacement of the bead is determined by the trap potential for a constant force on the bead. Modulation of the potential leads to modulation of the bead position in the trap and consequently the tubule length. Hence the response of the trapped bead to modulation depends on the response of vesicle-tubule system to the modulating force. The periodic modulation of the trap potential in our experiments results in force modulation since the bead is held away from the trap centre by the extended membrane tubule; refer to Figure 2.14. The response would therefore be determined by the force on the bead due to the tubule.

The system response was measured by the amplitude of bead oscillations as a function of frequency. In Figure 2.15 we plot the response (the amplitude of bead oscillations) as a function of the frequency of trap modulation for a constant tubule extension of 5μm in the saturation regime of the force-extension curve. The voltage outputs of the quadrant detector amplifiers are input to the lock-in amplifier. The time constant of the lock-in filter was set to achieve a good sampling even at the longest time period corresponding to the lowest frequency of modulation. The frequency was varied from 1Hz to 200Hz in steps of 1Hz; with a wait time of 5s before the data was recorded after a step change in frequency. Also

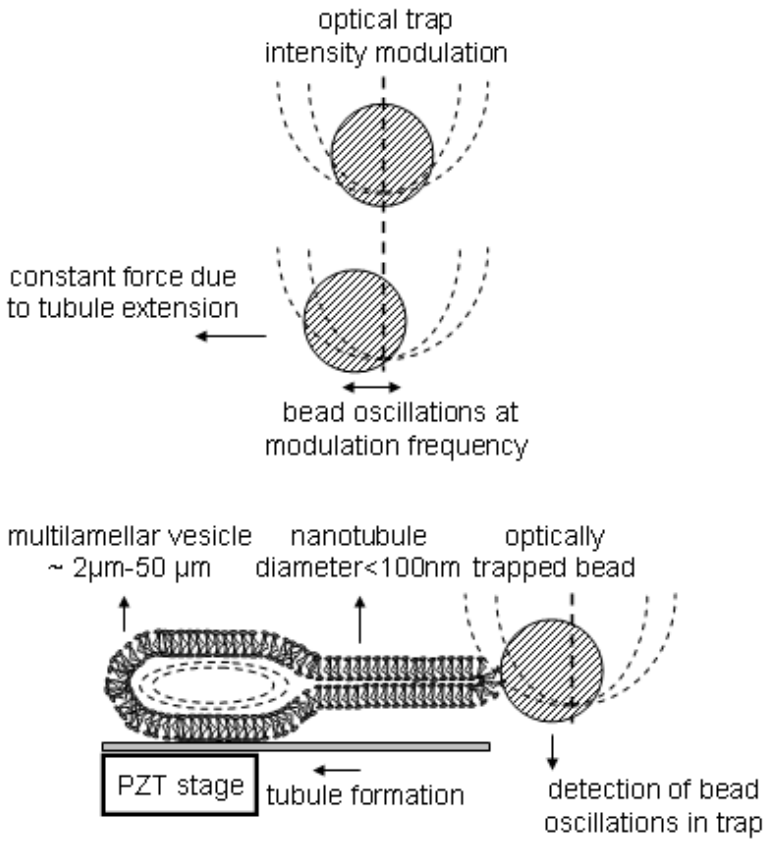

Figure 2.14

Experimental schematic of tubulation dynamics studied using an intensity modulated optical trap. The response of the trapped bead to the intensity modulation is determined by the constant force on the bead due to the tubule extension.

shown is the response amplitude of a trapped bead that is not anchored to the tubule. The response amplitude decreases with the modulation frequency as expected due to increased damping at higher frequencies, as shown in Figure 2.15. Overriding this decrease in response we observed three broad but measurable peaks in the response amplitude vs. frequency curve, at ~20Hz, ~70Hz and ~140Hz with the response amplitudes (a.u.) being ~0.75, ~0.3 and ~0.15 respectively. Higher frequencies of modulation gave very low response values, hence making measurements above 200Hz not possible. This reduction in the response amplitude at frequencies greater than 200Hz is due to viscous damping of the bead oscillations.

A possible explanation for the observed resonance may be due to the Rayleigh oscillations of the vesicle, driven by its surface tension. In that case, the resonant frequencies are given by [22],

$$\omega^2 = Al(l-1)(l+2)$$

$$A = \frac{\alpha}{\rho R^3}$$

where α is the surface-tension coefficient, ρ is the density and R the radius of the vesicle. Here l takes the values of positive integers. $l = 0$ is not allowed since this would result in increase in the volume of the drop and the fluid is incompressible. So is $l = 1$ which results in translational motion of the drop. The dominant even order oscillation frequencies are; for $l = 2, \omega_2^2 = 8A$, for $l = 4$, $\omega_4^2 = 72A$ and for $l = 6$, $\omega_6^2 = 240A$, which gives the frequency ratios 1, 3 and 5.5 respectively. The resonant peaks observed in the Figure 2.15 are approximately in the same ratio as noted above.

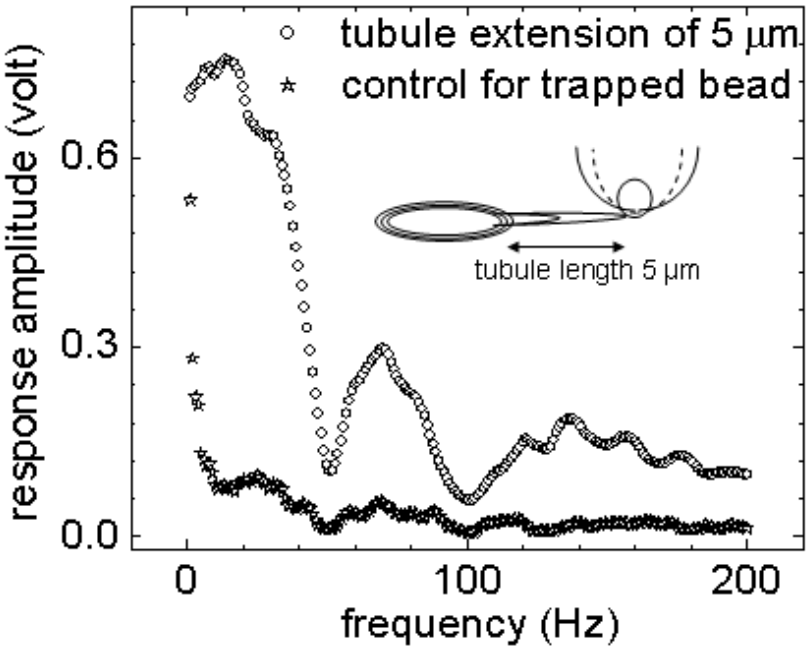

Figure 2.15

Response amplitude as a function of frequency of modulation at a tubule extension of 5µm (close to the onset of saturation in the force extension curve). The frequency is varied from 1 Hz to 200 Hz in steps of 1Hz, with a wait time of 5seconds before the data is recorded after a step change in frequency. The frequency response for a trapped bead not anchored to the tubule is also plotted as control.

Response amplitude as a function of tubule extension.

In Figure 2.16, we plot the amplitude of the response as a function of tubule extension. The mean value of the amplitude is recorded for each step increase in tubule length, with a wait time of 2s before each step change in extension (step size of 200nm), at different trap modulation frequencies (20Hz, 45Hz, 80Hz & 100Hz) on the same vesicle. The force-extension curve is also plotted to show that the saturation of the amplitude corresponds to the saturation in the force extension curve. The amplitude of the response increases with the tubule length and saturates at an extension in the range 2μm-5μm (varies for different vesicles). This is understood by noting that an increase in the force will increase the displacement of the bead from the trap centre. The modulation of the potential would now result in increase in the amplitude of the bead oscillation. In the saturation region of the force extension curve, the displacement is almost constant resulting in the saturation of the response amplitude. The saturation values for different frequencies of modulation follow the response amplitude obtained in the frequency sweep measurements (Figure 2.15). Thus, for example, the response amplitude in the saturation regime decreases from 20Hz to 50Hz and again peaks at 80Hz.

At frequencies of 80Hz and 100Hz we see a resonance at the onset of saturation at tubule extensions of 3.5μm and 2.5μm respectively. This resonant enhancement of the response amplitude is at the transition from elastic to the viscoelastic region of the force-extension curve. The peak height is maximal at 80Hz and decreases at 100Hz (Figure 2.16), revealing a characteristic frequency range where the time scale of membrane flow presumably matches the oscillation in the bead displacement. Such resonant enhancement is not observed for frequencies greater than 100Hz. The frequencies at which we observe these resonances correspond to a time scale ~10ms. The force curves are obtained at much slower rates allowing the system to reconfigure. The dependence on the frequency of modulation may be determined by the membrane tension of the vesicle as discussed in the previous section. Rate dependent tubule extrusion studies on biological cell membranes as well as artificial vesicles show that the diameter of the tubule depends on the tubule membrane tension [21]. Also in these experiments the tubule exhibited thinning with increased tubule length. The membrane tension and the bending stiffness determine the dependence of the tubule radius with extension [23].

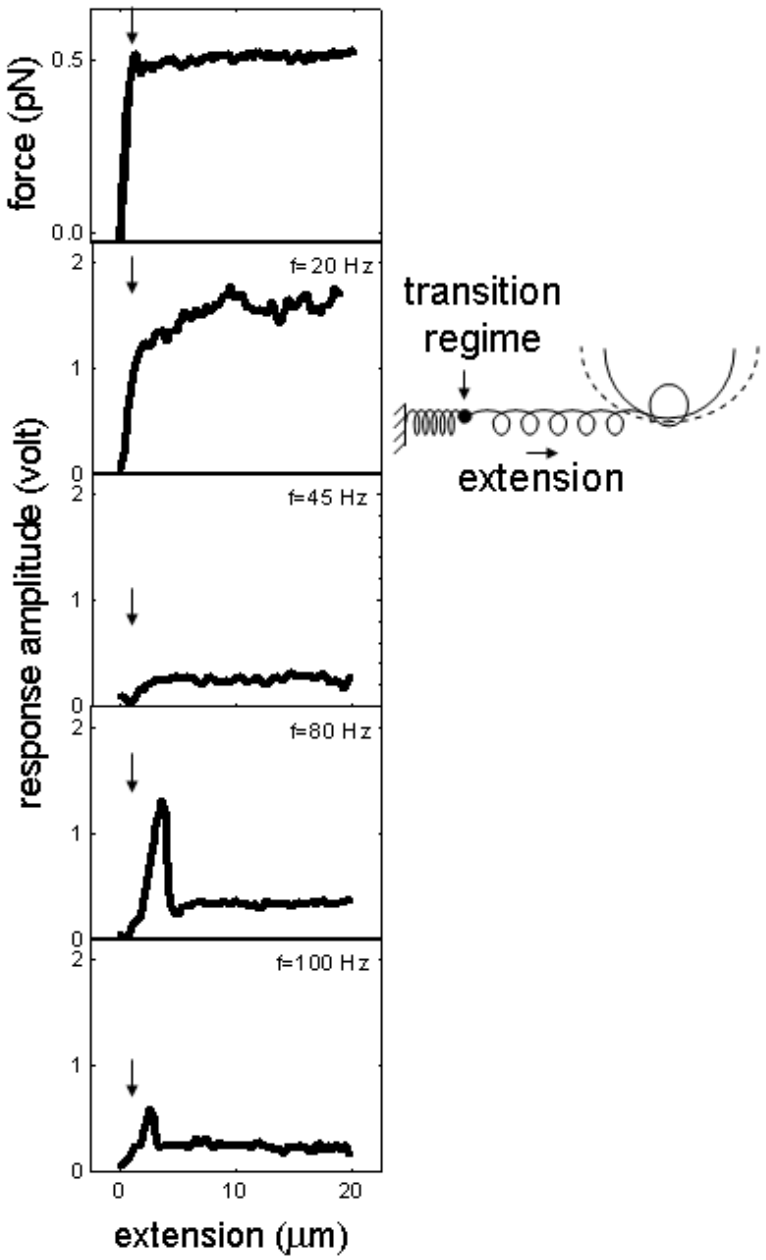

Figure 2.16

Response amplitude as a function of tubule extension for modulation frequencies of 20 Hz, 45 Hz, 80 Hz & 100 Hz. The dc force-extension curve is also plotted to depict the correlation between the onset of flow regime and the resonance in the response amplitude.

In section 2.4.2 which discussed the stiffness of the membrane tubule, we saw that the tubule does not contribute to the tension of the vesicle. This is validated by the measurement of the histograms position of time series; standard deviation of ~51nm for the bead attached at the end of the tubule and ~54nm for the trapped bead. In that case the nanotubule is just a probe of the vesicle response since the tubule does not contribute to the tension of the vesicle. Alternatively, the flow of membrane into the tubule, and hence the process of tubule formation from the vesicle, may be frequency dependent. Our system being a multilamellar vesicle the membrane flow across the bilayers at the junction of the tubule where the tension is maximum, could cause the tubule extension. Trans-bilayer movement of lipid molecules has been observed in unilamellar vesicles when deformed by a force [24, 25]. The interleaflet transport of the lipid molecules driven by mechanical stress, for example as in the case of tubule extraction, is also shown to be facilitated by defects in the membrane bilayers [26]. Our results suggest that the flow of membrane in the multilamellar vesicles studied may be caused by inter-bilayer membrane transport due to defects in the multilayer system. At the junction of the tubule-vesicle, the applied tension leads to the transport of the membrane across the bilayers. Our results suggest a timescale of ~10ms, the flow being enhanced at these timescales.

2.5 Conclusions

In conclusion to this chapter we have studied a regime of viscoelastic flow of membrane material in multilamellar vesicle system. The optical trap used in these experiments was sensitive to sub-picoNewton forces. We have measured the force ~(0.4-0.8)pN for forming a nanotubule of radius <100nm from a vesicle with tension ~10^{-19}N/m. We have used a methodology where the vesicle-tubule system is forced due to the periodic trap modulation. Frequency specific resonant behavior of the vesicle-tubule system was observed. We suggest that this methodology could be applied to measure the dynamic reorganization of cell membrane which happen at small time scales. The reorganization of the membrane proteins and lipids are known to form dynamically at length scales of the order of hundreds of nanometers, controlling the local membrane properties. The conventional optical trap is not sensitive to small changes in the membrane tension due to the Brownian fluctuations. Such tubular connections between cells are used for inter-cellular transport of proteins and even organelles [27]. Since the cargo length scales are of the same order as the channel, the three dimensional diffusion can no longer be applied. The artificial system of tubules between vesicles provides a minimal design to study such transport.

2.6 References

1. Sciaky N., Presley J., Smith C., Zaal K. J. M., Cole N., Moreira J. E., Terasaki M., Siggia E. and Lippincott-Schwartz J. *J. of Cell Biol.* **139**, 1137 (1997).

2. Roux A., Cappello G., Cartaud J., Prost J., Goud B. and Bassereau P. *Proc. Natl. Acad. Sci.* **99**, 5394 (2002).

3. Leduc C., Campas O., Zeldovich K. B., Roux A., Jolimaitre P., Bourel-Bonnet L., Goud B., Joanny Jean-Francois, Bassereau P. and Prost J. *Proc. Natl. Acad. Sci.* **101**, 17096 (2004).

4. Upadhyaya A. and Sheetz M. P. *Biophys. J.* **86**, 2923 (2004).

5. Raucher D. and Sheetz M. P. *Biophys. J.* **77**, 1992 (1999).

6. Cuvelier D., Derenyi I., Bassereau P. and Nassoy P. *Biophys. J.* **88**, 2714 (2005).

7. Waugh R. E. and Hochmuth R. M. *Biophys. J.* **52**, 391 (1987).

8. Hocumuth R. M. and Evans E. A. *Biophys. J.* **39**, 71 (1982).

9. Hocumuth R. M., Wiles H. C. , Evans E. A. and McCown J. C. *Biophys. J.* **39**, 82 (1982).

10. Bo L. and Waugh R. E. *Biophys. J.* **55**, 509 (1989).

11. Koster G., Cacciuto A., Derenyi I., Frenkel D and Dogterom M. *Phys. Rev. Lett.* **94**, 068101 (2005).

12. Soni G. V., Hameed F. M., Roopa T. and Shivashankar G. V. *Curr. Sci.* **83**, 1464 (2002).

13. Shivashankar G. V., Stolovitzky G. and Libchaber A. *Appl. Phys. Lett.* **73**, 291 (1998).

14. Dubois M., Zemb Th., Fuller N., Rand R. P. and Parsegian V. A. *J. of Chem. Phys.* **108**, 7855 (1998).

15. Hefrich W, *Z. Naturforsch C.* **28**, 693 (1973).

16. Derényi I., Jülicher F. and Prost J. *Phy. Rev. Lett.* **88**, 238101 (2002).

17. Waugh R. E., Song J., Svetina S. and Zeks B. *Biophys. J.* **61**, 974 (1992).

18. Cuveleir D., Chiaruttini P., Bassereau P. and Nassoy P. *Europhys. Lett.* **71**, 1015 (2005).

19. Hwang W. C. and Waugh R. E. *Biophys. J.* **72**, 2669 (1997).

20. Bozic B., Svetina S., Zeks B. and Waugh R. E. *Biophys. J.* **61**, 963 (1992).

21. Rossier O., Cuveleir D., Puech P. H., Derenyi I., Buguin A., Nassoy P. and Brochard-Wyart F. *Langmuir*. **19**, 575 (2003).

22. Landau L.D. and Lifshitz E. M., Fluid Mechanics. Pergamon Press, New York (1959).

23. Powers T. R., Huber G. and Goldstein R. E. *Phys. Rev. E*. **65**, 041901 (2002).

24. Raphael R. M. and Waugh R. E. *Biophys. J.* **71**, 1374 (1996).

25. Svetina S., Waugh R. E. and Raphael R. M. *Eur. Biophys. J.* **27**, 197 (1998).

26. Raphael R. M., Waugh R. E., Svetina S. and Zeks B. *Phys. Rev. E*. **64**, 051913 (2001).

27. Rustom A., Saffrich R., Markovic I., Walther P. and Gerdes H. *Science* **303**, 1007 (2004).